Superficies y Vacío 16(3), 12-17, septiembre de 2003 ©*Sociedad Mexicana de Ciencia de Superficies y de Vacío*

Enhanced non steady photo-electromotive force in p-i-n structures

Eliseo Hernández Hernández ,Carlos M. García Lara, Rubén Ramos-García
Instituto Nacional de Astrofísica, Óptica y Electrónica
Coordinación de óptica, Apdo. postal 51 y 216, Tonantzintla, Puebla, México

John A Coy , Michael R. Melloch, David D. Nolte
Department of Physics, Purdue University
West Lafayette, Indiana, 47907

The Non-Steady State Photo-Electromotive Force (p-emf) consists in the generation of holographic currents. These currents are generated by an oscillatory interference pattern that impinges on the material. This technique is quite useful for electrical characterizations of the specimens; in addition to its usage for laser based ultrasound detection. The as-generated currents can be measured in plane or vertically. P^+-i-n^+ structures provide a natural way in which the vertical transport can be detected. P-emf was measured for first time to our knowledge in p^+-i-n^+ structures in which the intrinsic layer was grown as a superlattice of 150 periods of 100Å GaAs wells and 40Å $Al_{0.5}Ga_{0.5}As$ barriers at low temperature (310 °C); this multilayered region decreases up to thousands times the vertical mobility of the photocarriers; degrading the performance of the p-emf signal since the current is in direct relationship with the mobility of the photocarriers. A new design that overcomes this limit is proposed and grown for investigation of the holographic currents. A full optical and electrical characterization of the new structure is presented and discussed.

Keywords: Non steady state photo-electromotive force; P-i-n structure; GaAs; Superlattice; Low temperature growth

1. Introduction

The non-steady state photoelectromotive force (P-emf) was measured for first time by Trofimov [1]. This effect consist in the generation of a photocurrent induced by a nonuniform spatial light pattern vibrating at determined frequency in a photoconductive compensated material. In these materials the Fermi level has been pinned to the middle of the conduction band by incorporating deep traps. P-emf has been measured in a wide variety of materials such as sillenites [1-4] ($Bi_{12}SO_{20}$, $Bi_{12}TiO_{20}$, $Bi_{12}GeO$), ferroelectrics [5-8] ($BaTiO_3$, $KNbO_3$:Fe, $Sr_xBa_{1-x}Nb_2O_6$, $LiNbO_3$) and semi-insulating semiconductors such as GaAs, CdTe and InP [9]. In particular, GaAs has been used in quantum well configurations because of its photorefractive properties [10].

P-emf can be used for characterization of materials and for a wide variety of applications such as laser based ultrasound detection, mechanical vibrations sensing, spectral analysis, 2D image processing, just for mention some of them [11].

2. Growth structures

In this work we present results of p-emf measurements in two types of structures. Both were grown in a p^+-i-n^+ configuration by molecular beam epitaxy on n^+ substrates. The growth structures are shown in the figure 1; one of them, (Fig. 1a) has both a low temperature growth (LTG) and a superlattice as intrinsic region. The LTG layer turns the material semi-insulating due to the incorporation of excess As in the form of point defects during the growth [12]. These defects behave as trapping and recombination centers. The resistivity of this layer lies between 10^3-10^4 Ωcm [13]. The superlattice is conformed by a 150 periods of 100Å GaAs wells and 40Å AlGaAs barriers with a total thickness of 2.1μm. The superlattice enhances the electro-optic properties and sensitivity of the device [14]. In this work we do not use those properties. From bottom to top the first layer grown onto the substrate is for MBE porpouses only, the $Al_{0.5}Ga_{0.5}As$ is a stop etch layer, the AlAs layer, known as flash layer is grown to remove any gradient left at the bottom when chemical wet etch is carried on. The GaAs layer immediately above the flash layer works as a cap layer for preventing oxidation and on top of them (another is in the top of the structure) gold electrodes were evaporated. $Al_{0.5}Ga_{0.5}As$ layers were put onto the superlattice for buffering it.

The other structure in which p-emf measurements were carried out is shown in figure 1b. Notice the presence of two MTG (medium temperature growth) layers sandwiching the intrinsic region. These layers were as-grown in order to get the essential trapping centers density involved in the photo-emf mechanism. The intrinsic layer thickness was calculated taking into account the criteria design $1/\alpha < d < 2/\alpha$, where α is the absorption coefficient and d is the intrinsic layer thickness [15]. The resistivity of the 350°C layers lies between 10^4-10^5 Ωcm [13].

The structures were processed in two different ways. The one that has the superlattice in the intrinsic region was made as a transmission device because of the presence of the quantum wells. A detailed description of the processing procedures for the transmission device can be checked elsewhere [16]; while the structure that has only the intrinsic layer was made as a mesa structure. To define the structure several steps were necessary: photolithography

Growth Temperature	Layer	Doping	Thickness
350°C	p-GaAs	$1x10^{19}cm^{-3}$	2000Å
350°C	p-$Al_{0.3}Ga_{0.7}As$	$1x10^{18}cm^{-3}$	2000Å
310°C	150 period superlattice 100Å GaAs / 40Å $Al_{0.5}Ga_{0.5}As$ 0.2% excess As		
600°C	n-$Al_{0.3}Ga_{0.7}As$	$1x10^{17}cm^{-3}$	2000Å
600°C	n-GaAs	$1x10^{18}cm^{-3}$	500Å
600°C	n-AlAs		200A
600°C	n-$Al_{0.5}Ga_{0.5}As$	$1x10^{18}cm^{-3}$	5000A
600°C	n-GaAs	$1x10^{18}cm^{-3}$	0.75μm
	n^+ GaAs substrate 032995C		

(a)

Growth Temperature	Layer	Doping	Thickness
	p^+ GaAs	$1x10^{19}cm^{-3}$	0.1μm
350° C	i-$Al_{0.2}Ga_{0.8}As$		20nm
350° C	i-GaAs		0.2μm
	i-GaAs		1μm
350° C	i-GaAs		0.2μm
350° C	i-$Al_{0.2}Ga_{0.8}As$		20nm
	n^+ GaAs	$1x10^{18}cm^{-3}$	2μm
	n^+ AlAs	$1x10^{18}cm^{-3}$	20nm
	n^+ $Al_{0.5}Ga_{0.5}As$	$1x10^{18}cm^{-3}$	0.4μm
	n^+ GaAs	$1x10^{18}cm^{-3}$	0.5μm
	n^+GaAs substrate 041602		

(b)

Figure 1. Growth structures used for detecting P-emf signals in longitudinal configurations; a) P^+-i-n^+ structure with a superlattice and LTG region in the intrinsic region, b) P^+-i-n^+ structure with the intrinsic region sandwiched by two MTG layers.

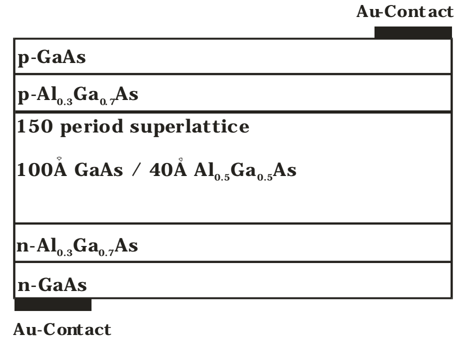

(a)

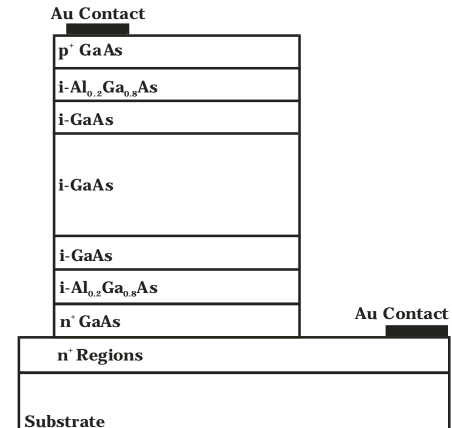

(b)

Figure 2. Schematic section of the finished devices. (a) IL134 sample made a transmission device. (b) EH13 device made as mesa structure.

was made to define the active area of the device, next, the mesa was created by etching down to the n^+ region, after this, photolithography was made again to define the windows where the electrodes were evaporated. As final step, lift-off was made in order to remove the photoresist that prevented the whole structure from suffering gold evaporation.

The device that has both an LTG and a superlattice in the intrinsic layer will be named IL134, while the one that does not have any superlattice in the intrinsic layer will be named EH13. An important open question is why the EH13 device with the MTG cladding required proton implantation in order to work. The MTG layers were designed to be sufficient to deplete the residual shallow defects in the as-grown GaAs layer, rendering the layer high resistivity. The carrier lifetimes would then have been long in the photoconductive layer, with consequently high vertical transport. The absence of any significant p-emf signal in the as-grown structures is most likely caused by a lack of spatial modulation in the space-charge, or alternatively described as fringe washout. This may arise because the diffusion transport length may have been too long for the fringe spacings used in this study, allowing the carriers to diffuse uniformly within the photonconductive layer. The proton implantation may have provided sufficiently shorter carrier lifetimes to reduce the in-plane diffusion and to maintain the spatial modulation of the charge carriers in the layer. The specimen was implanted at a dose of $H^+ = 1 \times 10^{13}cm^{-2}$ because this implantation level introduces a similar quantity of defects as an LTG layer [13].

The active areas of the devices are: $0.12cm^2$ for the IL134 sample and $0.04cm^2$ for the EH13 device.

P-emf can be measured in two different geometries. In one of them the photocurrent is paralel to the grating vector; this type of detection is called transverse configuration, in the other, the transport is perpendicular to the grating vector; this configuration is called longitudinal configuration. Both configurations can be seen in the figure 3.

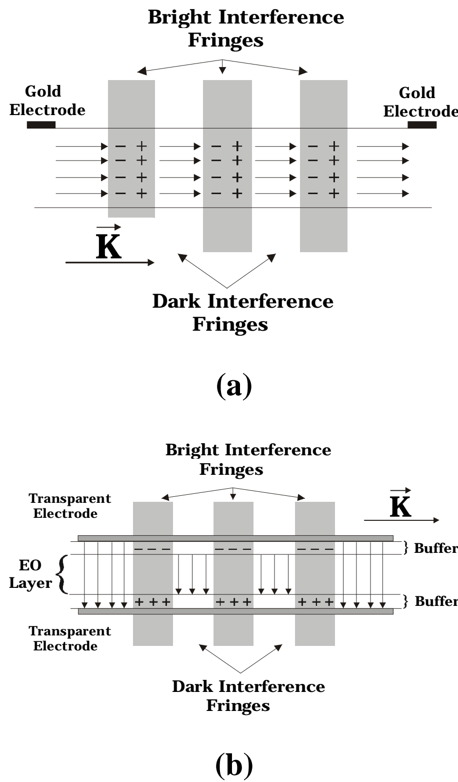

Figure 3. Geometries used for measuring P-emf signals; a) Tranverse configuration, b) Longiudinal configuration. $\vec{K}$ is the grating vector.

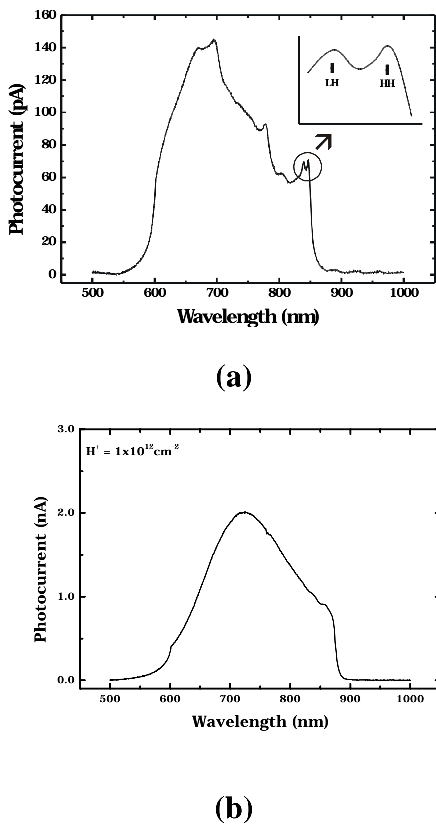

Figure 4. Spectral response of the devices used in the present work. a) IL134 sample. (b) EH13 sample.

3. Spectral Response

The optical absorption spectra of the used devices were obtained using the radiation from a quartz halogen lamp monochromated with an one-meter double-grating spectrometer. In the figure 4 can be seen the photocurrent spectra of the devices. Notice that for the quantum well structure the heavy and light hole excitonic peaks are well resolved around 840nm. This is because of the excitons confinement in the GaAs wells [17].

4. Photovoltage and photocurrent measurements

The used structures have a built-in potential because they are conformed of three different regions as it can be seen in the figure 5

This potential created by the difference in positions of the Fermi level in the p^+ and n^+ type regions and enhanced by the intrinsic layer presence can be detected performing photovoltage measurements as a function of the incident intensity on the sample. Flat band condition can be reached if the specimen is illuminated with sufficient energy. Devices response can provide fundamenteal issues for the p-emf behavior because the device has an inherent built-in potential that can be controlled changing the incident optical power. On the other hand, photocurrent measurements as a function of the ligth power provide information about the mobility-carrier lifetime product. The behavior of the photovoltage can be seen in the figure 6.

5. Experimental setup

In the figure 7 can be seen the experimental setup used for measuring the p-emf signals in the samples used. This consists of a modified Mach Zender interferometer; this version is extremely useful for characterizations requiring a wide spatial period range (5μm to 200μm); the mirror (M) enclosed in the gray box has two motion stages for accomplishing the required adjustments that sets the spatial period up. The laser radiation was supplied from a Verdi V-5, solid state, CW, high power, 532 laser pumped by a single diode module frequency doubled Nd. Vanadate (Nd:YVO). The laser beams that comes from the electro-optic modulator (EOM) and the lower left mirror are collimated by the microscope objectives (MO), pin holes and the positive lenses (L) for illuminating the sample with plane waves and in this way avoid any asymmetry introduced by the radiation impinging the sample.

The p-emf signal is taken from the load resistor (R_L), it goes to a PC passing through a lock-in amplifier. The motion stages and the lockin amplifier are controlled using the GPIB protocol which allows the user to get measurements with high reliability.

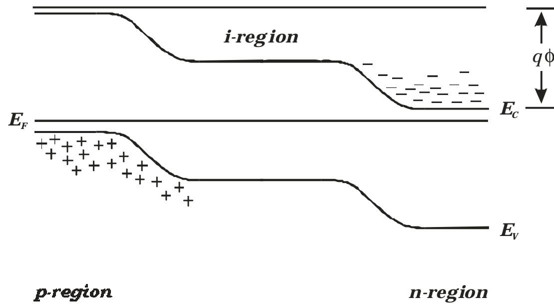

Figure 5. Bands diagram of a p-i-n structure.

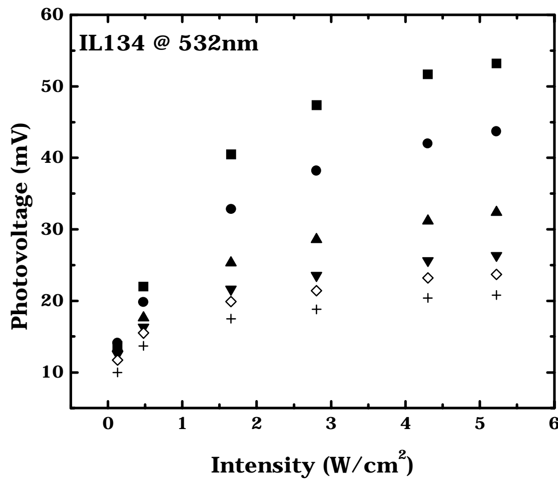

(a)

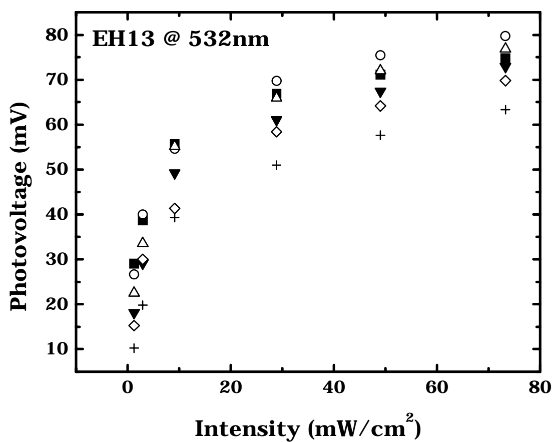

(b)

Figure 6. Photovoltage versus intensity for: (a) IL134 sample, (b)EH13 sample. ■,○,△,▼,◆ and ✚ are measurements for 100Hz, 200Hz, 400Hz, 700Hz, 1kHz and 2kHz.

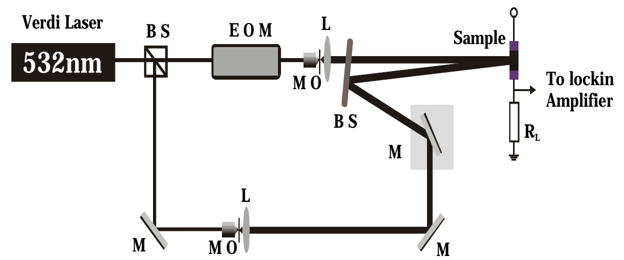

Figure 7. Optical setup used for measurements of the p-emf signal.

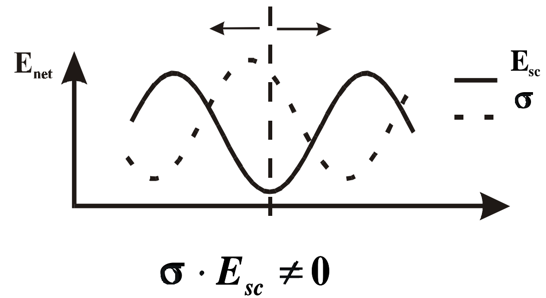

Figure 8. The photoconductivity peak pattern oscillates around the valleys of the space charge pattern. The detected p-emf signal oscillates at the second harmonic.

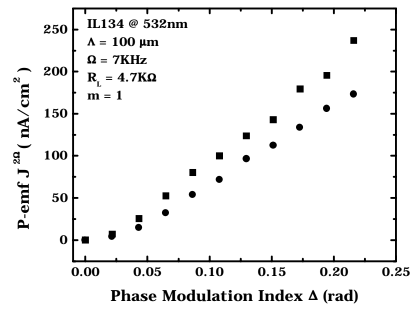

(a)

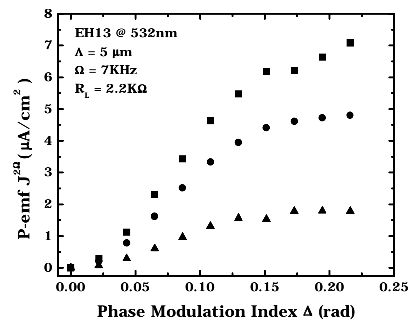

(b)

Figure 9. P-emf signal versus phase modulation index. In the figure (a) squares are for I_1 = 55mW/cm^2, and circles for I_2 = 17.5mW/cm^2. For figure (b) squares are for I_3 = 5mW/cm^2, circles for I_4 = 3.45mW/cm^2 and triangles for I_5=2.86mW/cm^2; for these figures the modulation indexes are m_1=1, m_2=0.8 and m_3=0.5 respectively.

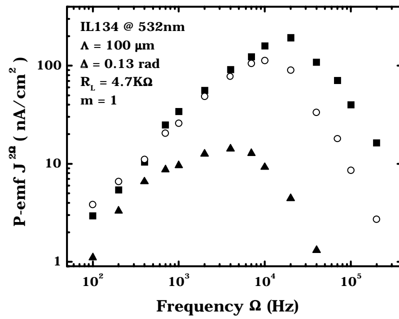

(a)

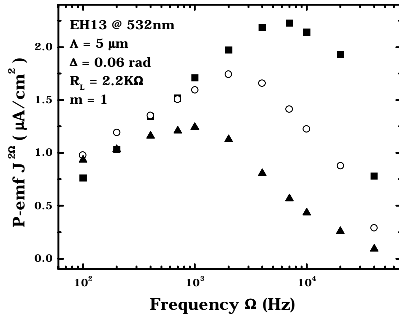

(b)

Figure 10. P-emf signal versus frequency modulation. In the figure (a) squares are for I_1 = 55mW/cm^2, circles for I_2 = 17.5mW/cm^2 and triangles for I_3 = 2mW/cm^2. For figure (b) squares are for I_4 = 5mW/cm^2, circles for I_5 = 1.5mW/cm^2 and triangles for I_6 = 0.5mW/cm^2.

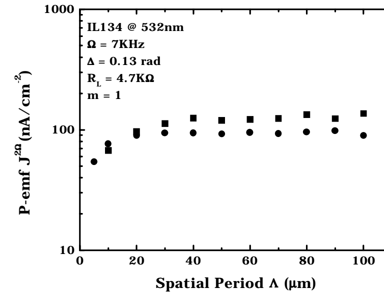

(a)

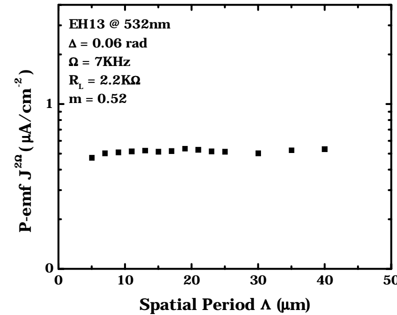

(b)

Figure 11. P-emf signal versus spatial period. In the figure (a) squares are for I_1 = 55mW/cm^2, circles for I_2 = 17.5mW/cm^2. For figure (b) I_3 = 3mW/cm^2.

It is quite important to mention that the signal was measured in second harmonic; this was required because the photoconductivity peak pattern oscillates around the valley of the space-charge field pattern as it can be seen in the figure 8. Furthermore, the transport in the structures is not in plane in this type of configuration.

6. PhotoEMF measurements

The performance of the p-emf signal versus the modulation index for the samples IL134 and EH13 is shown in the figure 9. For the IL134 sample the behavior is quadratic for the whole range of index modulation used for these experiments; this is not the case for the sample EH13 where a quadratic behavior is seen until to a phase modulation index of 0.11 radians. After this value, a saturation level appears for the EH13; in fact the plots in circles and upper triangles in figure 8b show a clearly saturation region. Notice that the signal amplitude for the EH13 sample is roughly one order of magnitude larger than for the IL134 sample.

P-emf response as a function of the frequency shows a band-pass filter performance. The lower cutoff frequencies shown in the figure 10 are associated with the inverse of the dielectric relaxation time of the specimens; both IL134 and EH13 samples have a similar behavior as the total incident optical power on them is increased. The second cutoff frequency of the devices is associated with its respective RC constant; where R is the total equivalent resistance and C is the capacitance of the sample.

Spatial period dependence of p-emf can be seen in the figure 11. The signal is completely different to conventional p-emf reponse. Conventional behavior follows a linear increasing as the spatial period increases. Then, the signal reaches its maximum when the spatial period that is the spatial frequency reciprocal equals the diffusion length of the device; after this maximum the signal decreases as the reciprocal of the spatial period. This is not the case for the H13 device and this may be a consequence of the mechanism that dominates the transport in these structures. Therefore, it is good to remember here that we have an structure that already has an applied voltage across it, this is the built-in potential of a p-i-n structure which was mentioned at the beginning of the paper. This potential must be playing a critical roll for the device performance. In addition this potential can be modulated changing the total incident power.

7. Conclusions

We have shown two different types of structures, one that has a superlattice in the intrinsic layer and other that does not have any superlattice for measuring p-emf signals. P-emf was increased for around one order of magnitude in the

device that does not have any superlattice in the intrinsic layer. The theory that justifies the obtained results is in progress. As it was pointed out in these type of structures the dominant mechanism is the drift one because of presence of the built-in potential in the structure. This mechanism is a key roll in the performing of the structure used in the present work.

8. Acknowledgements

Eliseo Hernández Hernández is very grateful with the grant given by CONACyT and by the hosting of the Professor D. D. Nolte in the Purdue University.

References

[1] G. S., Trofimov, S. I. Stepanov, Sov. Phys. Solid State **28**, 1559, (1986).
[2] M. P. Pretov, S. I. Stepanov, and G. S. Trofimov, Sov. Tech. Phys. Lett. **12**, 379 (1986).
[3] A. Sokolov and S. I. Stepanov, J. Opt. Soc. Am B. **10**, 1483 (1993).
[4] S. L. Sochava, K. Buse, and E. Krätzig, Phys. Rev. B. **51**, 4684 (1995).
[5] S. Sochava, K. Buse and E. Krätzig, Opt. Commun. **98**, 265 (1993).
[6] Krumins and P. Gunter, Phys. Statis Solidi A **63**, K111 (1981).
[7] N. Korneev, D. Mayorga, S. Stepanov, A. Gerwens, K. Buse, and E. Kratzig, Opt. Commun. **146**, 215 (1998).
[8] Veenhuis, K. Buse, E. Kratzig, N. Korneev, and D. Mayorga, J. Appl. Phys. **86**, 2389 (1999).
[9] G. S. Trofimov, S. I. Stepanov, M. P. Petrov, and M. V. Krasin'kova, Sov. Tech. Phys. Lett. **13**, 108 (1987).
[10] C. C. Wang, R. A. Linke, D. D. Nolte, M. R. Melloch, and S. Trivedi, Appl. Phys. Lett. **70**, 2034 (1997).
[11] H. S. Nalwa, Handbook of Advanced Electronic and Photonic Materials and Devices, Vol. II, Academic Press.
[12] M. Kaminska, E. R. Weber, Z. Liliental-Weber, R. Leon, and Z. U. Rek, J. Vac. Sci. Technol. **B7**, 712 (1989).
[13] J. K Luo, H. Thomas, D. V. Morgan, J. Appl. Phys., **79**, 3622, (1996).
[14] D. S., Chelma, Physics and Fabrication of Microstructures and Microdevices, Proceedings of the Winter School. Springer-Verlag, 289, (1986).
[15] S. M. Sze, Physics of Semiconductor Devices, 2nd., Edition, Wiley-Interscience Publication.
[16] W. R. Headly, Master of Science Thesis, Purdue University, August 2001.
[17] D. A. B. Miller, Int. J. H. Sp. Electron., **1**, 19, (1990).